

Self-similar Solution of Hot Accretion Flow with Thermal Conduction and Anisotropic Pressure

AMIN MOSALLANEZHAD ¹, FATEMEH ZAHRA ZERAATGARI ¹, LIQUAN MEI ¹ AND DE-FU BU ²

¹*School of Mathematics and Statistics, Xi'an Jiaotong University, Xi'an, Shaanxi 710049, PR China*

²*Shanghai Astronomical Observatory, Chinese Academy of Sciences, Shanghai 200030, China*

ABSTRACT

We explore the effects of anisotropic thermal conduction, anisotropic pressure, and magnetic field strength on the hot accretion flows around black holes by solving the axisymmetric, steady-state magnetohydrodynamic equations. The anisotropic pressure is known as a mechanism for transporting angular momentum in weakly collisional plasmas in hot accretion flows with extremely low mass accretion rates. However, anisotropic pressure does not extensively impact the transport of the angular momentum, it leads to shrinkage of the wind region. Our results show that the strength of the magnetic field can help the Poynting energy flux overcomes the kinetic energy flux. This result may be applicable to understand the hot accretion flow in the Galactic Center Sgr A* and M87 galaxy.

Keywords: Black holes – High energy astrophysics – Astrophysical black holes – Supermassive black holes – Accretion – Magnetohydrodynamics

1. INTRODUCTION

According to the temperature of the accretion flow, black hole accretion disks can be divided into two broad types; cold and hot. Intensive analytical studies and simulations have been done on hot accretion flows, since the pioneer study of Narayan & Yi 1994. It is well known that variety of accreting systems in the universe with low mass accretion rate such low-luminosity active galactic nuclei (LLAGNs) as well as black hole X-ray binaries in the quiescent and hard states can be explained by hot accretion flow model (Yuan & Narayan 2014). Indeed, hot accretion flow is an efficient model to describe the accretion flow around majority of nearby galaxies with extremely low-luminosity including our galactic center, Sagittarius A* (Sgr A*) and M87.

Based on observations of black hole X-ray binaries and LLAGNs, outflow (wind and jet) can be launched from hot accretion flow (Tombesi et al. 2010, 2014; Crenshaw & Kraemer 2012; Wang et al. 2013; Cheung et al. 2016; Ma et al. 2019). Wind can push the gas around the black hole outward and affectively change the black hole accretion rate in hot accretion systems. Wind is not only a key ingredient of accretion flows which can impact on

their dynamics and structure, but feedback of the wind on the surrounding medium can also play a major role in the formation and evolution of galaxies (Fabian 2012; Kormendy & Ho 2013; Naab & Ostriker 2017).

Three different wind-launching mechanics have been proposed, including thermally driven (Begelman et al. 1983; Font et al. 2004; Luketic et al. 2010; Waters & Proga 2012), magnetically driven (Blandford & Payne 1982; Lynden-Bell 1996, 2003), and radiation-driven wind (Murray et al. 1995; Proga et al. 2000; Proga & Kallman 2004; Nomura & Ohsuga 2017). In terms of hot accretion flow, the first two mechanisms play a major role in producing wind since the radiation is negligible (Yuan & Narayan 2014). To investigate the existence of wind in a hot accretion flow, a large number of hydrodynamical (HD) and magnetohydrodynamical (MHD) numerical simulations have been carried out so far (e.g., Stone et al. 1999; Igumenshchev & Abramowicz 1999; Stone & Pringle 2001; Hawley et al. 2001; Machida et al. 2001; Pen et al. 2003; De Villiers et al. 2003, 2005; Yuan & Bu 2010; Pang et al. 2011; McKinney et al. 2012; Narayan et al. 2012; Li et al. 2013; Yuan et al. 2012a,b, 2015; Bu & Zan 2018; Inayoshi et al. 2018, 2019).

Hot accretion flows with very low mass accretion rate are in fact virially hot and low-density plasmas (Narayan et al. 1998; Quataert 2003; Yuan & Narayan 2014). Since the density is very low, the plasma is collisionless, i.e., the Coulomb mean free path is many orders of mag-

nitude larger than the system size. Therefore, the electrons should move large distance to exchange the energy with other particles. In such a case, thermal conduction is important and can significantly change the dynamics of the accretion flow. On the other hand, it is well known that the magnetorotational instability (MRI) is a mechanism to induce magnetohydrodynamic turbulence for driving the angular momentum outward in accretion flows (Balbus & Hawley 1991). Consequently, the MHD equations of hot accretion flow should include thermal conduction. Moreover, the ions mean free path is also quite large compare to the larmor radius in hot accretion flow with low mass accretion rate. The ions move along the field lines. Therefore, the pressure should be anisotropic. We can treat the anisotropic pressure as a perturbation to the ideal MHD and include it to the MHD equations.

There are several analytical investigations based on the self-similar assumption that probe the magnetic field effects in hot accretion flows (Akizuki & Fukue 2006; Abbassi et al. 2008; Zhang & Dai 2008; Bu et al. 2009; Mosallanezhad et al. 2014; Samadi et al. 2017; Bu & Mosallanezhad 2018; Deng & Bu 2019). In practice, the analytical studies are powerful tools to understand the physical properties of inflow and wind from accretion flow. The reasons are as follows: (1) global numerical simulations of accretion flow are expensive and time-consuming because of the complex physics involved such as dissipation and magnetic field, (2) analytical techniques are straightforward to check the dependency of the results on the variety of physical input parameters.

In the present study, we also adopt radially self-similar assumption and solve the MHD equations of hot accretion flow in the vertical direction. We mainly focus on two extreme cases of magnetic field, namely weak and strong field. The magnetic field strength will be initialized by the usual plasma beta definition as $\beta_0 = p_{\text{gas}}/p_{\text{mag}}$, where p_{gas} and p_{mag} represent the gas and magnetic pressure at the equatorial plane, respectively. Our main goal is to study the influence of the anisotropic pressure, magnetic field strength and thermal conduction on the properties of the inflow and wind. More precisely, we examine how the physical input parameters such as thermal conductivity coefficient and initial plasma beta change the inflow and wind regions of the hot accretion flow. We also investigate the mass-flux weight properties of wind from hot accretion flow in both weak and strong field cases.

The remainder of the manuscript is organized as follows. In Section 2, the basic equations, physical assumptions, self-similar solutions, and the boundary conditions will be introduced. The numerical results of weak and

strong magnetic field cases will be presented in details in Section 3. Finally, we will provide the summary and discussion in Section 4.

2. NUMERICAL METHOD AND ASSUMPTIONS

2.1. Basic Equations

The basic equations of the hot accretion flow with extremely low-luminosity in the presence of viscosity, magnetic field, anisotropic pressure and thermal conduction can be described as,

$$\frac{d\rho}{dt} + \rho \nabla \cdot \mathbf{v} = 0, \quad (1)$$

$$\rho \frac{d\mathbf{v}}{dt} = -\rho \nabla \psi - \nabla p_{\text{gas}} + \nabla \cdot \boldsymbol{\sigma} + \frac{1}{c} (\mathbf{J} \times \mathbf{B}) + \nabla \cdot \boldsymbol{\Pi}, \quad (2)$$

$$\rho \frac{de}{dt} - \frac{p_{\text{gas}}}{\rho} \frac{d\rho}{dt} \equiv Q^+ + \nabla \cdot \mathbf{Q}_c - \boldsymbol{\Pi} : \nabla \mathbf{v}, \quad (3)$$

$$\frac{\partial \mathbf{B}}{\partial t} = \nabla \times \left(\mathbf{v} \times \mathbf{B} - \frac{4\pi}{c} \eta \mathbf{J} \right), \quad (4)$$

$$\nabla \cdot \mathbf{B} = 0. \quad (5)$$

In the above equations, ρ is the mass density, \mathbf{v} is the velocity, $\psi = -GM/r$ is the Newtonian potential (where G is the gravitational constant, M is the mass of the central black hole, and r is the distance from the black hole), p_{gas} is the gas pressure, $\boldsymbol{\sigma}$ is the viscous stress tensor, $\mathbf{J} = c(\nabla \times \mathbf{B})/4\pi$ is the current density (where c is the speed of light), \mathbf{B} is the magnetic field, $\boldsymbol{\Pi}$ is anisotropic pressure, e is the gas internal energy, Q^+ is the total heating due to viscous and magnetic dissipation, \mathbf{Q}_c is the thermal conduction, and η is the magnetic diffusivity. The $d/dt \equiv \partial/\partial t + \mathbf{v} \cdot \nabla$ denotes the Lagrangian or comoving derivative. The equation of state of the ideal gas is assumed as $p_{\text{gas}} = (\gamma - 1)\rho e$, with $\gamma = 5/3$ being the adiabatic index. In fact, in accreting systems Maxwell stress associated with MHD turbulence driven by MRI (Balbus & Hawley 1998) can transfer the angular momentum outward. Following the MHD numerical simulations, we decompose the magnetic field into a large-scale component and a turbulent component. The magnetic field, \mathbf{B} , in the above equations represents the large-scale component. The effects of turbulence are described by the viscosity terms of the momentum and the energy equations. Both components can transport the angular momentum outward and produce heat. Following numerical simulations of hot accretion flow, Stone et al. 1999; Yuan et al. 2012b, we assume the azimuthal

component of the viscous stress tensor, $\sigma_{r\phi}$, is the dominant component. This component is written as

$$\sigma_{r\phi} = \rho\nu_1 r \frac{\partial}{\partial r} \left(\frac{v_\phi}{r} \right), \quad (6)$$

where ν_1 is the kinematic viscosity coefficient which is evaluated as,

$$\nu_1 = \frac{\alpha_1}{\rho\Omega_K} (p_{\text{gas}} + p_{\text{mag}}), \quad (7)$$

where $\Omega_K (\equiv GM/r^3)^{1/2}$ is the Keplerian velocity, α_1 is the viscosity parameter, and $p_{\text{mag}} = |\mathbf{B}|^2/(8\pi)$ is the magnetic pressure. The heating rate Q^+ in equation (3) is decomposed into two components, i.e., the viscous heating and the magnetic field dissipation heating as,

$$Q^+ = Q_{\text{vis}} + Q_{\text{res}}, \quad (8)$$

with

$$Q_{\text{vis}} = \nabla \mathbf{v} : \boldsymbol{\sigma}, \quad (9)$$

$$Q_{\text{res}} = \frac{4\pi}{c^2} \eta \mathbf{J}^2. \quad (10)$$

Here, the magnetic diffusivity can be set as $\eta = \eta_0/(\rho\Omega_K) [p_{\text{gas}} + p_{\text{mag}}]$ to satisfy the self-similar solutions in the radial direction. Following the numerical simulations (e.g., [Braginskii 1965](#); [Balbus 2004](#); [Chandra et al. 2015](#)), we model the anisotropic pressure Π with an anisotropic viscosity,

$$\Pi = -3\rho\nu_2 \left[\hat{\mathbf{b}}\hat{\mathbf{b}} : \nabla \mathbf{v} - \frac{\nabla \cdot \mathbf{v}}{3} \right] \left[\hat{\mathbf{b}}\hat{\mathbf{b}} - \frac{\mathbf{I}}{3} \right], \quad (11)$$

where $\hat{\mathbf{b}} = \mathbf{B}/|\mathbf{B}|$ is a unit vector in the direction of magnetic field, and \mathbf{I} is the unit tensor. The anisotropic viscosity coefficient ν_2 is written as,

$$\nu_2 = \frac{\alpha_2}{\rho\Omega_K} (p_{\text{gas}} + p_{\text{mag}}). \quad (12)$$

The hot accretion flow is taken to be axisymmetric and steady state ($\partial/\partial\phi = \partial/\partial t = 0$). We adopt spherical polar coordinates (r, θ, ϕ) to solve the Equations (1)-(5). To avoid complexity due to considering all components of magnetic field, in our current analytical study, we assume only toroidal component of the field as

$$\mathbf{B} = B_\phi(r, \theta) \mathbf{e}_\phi, \quad (13)$$

which automatically satisfies $\nabla \cdot \mathbf{B} = 0$ ¹. With the help of the above assumptions, the three components of the current density, \mathbf{J} , can be read as

$$J_r = \frac{1}{r \sin \theta} \frac{\partial}{\partial \theta} (B_\phi \sin \theta), \quad (14)$$

$$J_\theta = -\frac{1}{r} \frac{\partial}{\partial r} (r B_\phi), \quad (15)$$

$$J_\phi = 0. \quad (16)$$

By considering toroidal component of the magnetic field, the anisotropic tensor can be reduced to

$$\Pi = \begin{bmatrix} \Pi_{rr} & 0 & 0 \\ 0 & \Pi_{\theta\theta} & 0 \\ 0 & 0 & \Pi_{\phi\phi} \end{bmatrix}, \quad (17)$$

with

$$\begin{aligned} \Pi_{rr} = \Pi_{\theta\theta} = -\frac{1}{2} \Pi_{\phi\phi} = \rho\nu_2 \left[\frac{v_r}{r} + \frac{v_\theta}{r} \cot \theta \right. \\ \left. - \frac{1}{3r^2} \frac{\partial}{\partial r} (r^2 v_r) - \frac{1}{3r \sin \theta} \frac{\partial}{\partial \theta} (\sin \theta v_\theta) \right]. \end{aligned} \quad (18)$$

In the MHD case, thermal conductivity is mostly anisotropic being suppressed in the direction transverse to the magnetic field. The form of the thermal conduction can be written as

$$\mathbf{Q}_c = \kappa \nabla T, \quad (19)$$

where T is the gas temperature and κ is the thermal conduction coefficient. Although the saturated form of the thermal conductivity is appropriate for hot accretion flows we adopt a standard form of thermal conduction in which the heat flux depends linearly on the local temperature gradient. Consequently, the radial dependency of the thermal conductivity coefficient κ is considered to be a power-law function of radius to preserve radial self-similarity, i.e., $\kappa(r) = \kappa_0 r^{1/2-n}$, where n is the density index (see [Tanaka & Menou 2006](#) and [Khajenabi & Shadmehri 2013](#) for more details). By substituting all the above assumptions and definitions into Equations (1)-(5), we obtain partial differential equations (PDE) presented in Appendix A.

¹ In future study, we relax this assumption and consider all components of the magnetic field to show the role of nonzero vertical magnetic flux.

2.2. Self-similar Solutions

Based upon the numerical HD and MHD simulations of hot accretion flow, time-averaged inflow and outflow mass accretion rates decrease with radius due to the existence of wind (Stone et al. 1999; Yuan et al. 2012a,b). Consequently, their results show that density profile becomes flatter than the case with constant mass accretion rate, in the range of $10r_s < r < 100r_s$ (far away from the strong gravity of central black hole and also outer boundary conditions), where r_s is the Schwarzschild radius. In this study, following the numerical simulations, we consider radial power-law form for the physical variables including density to remove the radial dependency of the variables. To do so, we adopt the following self-similar solutions in the radial direction by adopting a fiducial radius r_0 . The solutions can be written as

$$\rho(r, \theta) = \rho_0 \left(\frac{r}{r_0} \right)^{-n} \rho(\theta), \quad (20)$$

$$v_r(r, \theta) = v_0 \left(\frac{r}{r_0} \right)^{-1/2} v_r(\theta), \quad (21)$$

$$v_\theta(r, \theta) = v_0 \left(\frac{r}{r_0} \right)^{-1/2} v_\theta(\theta), \quad (22)$$

$$v_\phi(r, \theta) = v_0 \left(\frac{r}{r_0} \right)^{-1/2} v_\phi(\theta), \quad (23)$$

$$c_s(r, \theta) = v_0 \left(\frac{r}{r_0} \right)^{-1/2} c_s(\theta), \quad (24)$$

$$B_\phi(r, \theta) = B_0 \left(\frac{r}{r_0} \right)^{-(n/2)-(1/2)} b_\phi(\theta), \quad (25)$$

where r_0 , ρ_0 , v_0 [$= \sqrt{GM/r_0}$], and B_0 [$= v_0 \sqrt{4\pi\rho_0}$] are the units of length, density, velocity, and magnetic field, respectively. The ordinary differential equations (ODEs) can be derived by substituting the above self-similar solutions into the PDEs (A1)–(A6). The coupled system of ODEs is presented in Appendix B. The ODEs (B7)–(B12) consist of six physical variables: $v_r(\theta)$, $v_\theta(\theta)$, $v_\phi(\theta)$, $\rho(\theta)$, $c_s(\theta)$, $b_\phi(\theta)$ as well as their derivatives.

2.3. Boundary Conditions

All physical variables are assumed to be even symmetric, continuous, and differentiable at equatorial plane. Hence, $v_r(\theta) = v_r(\pi - \theta)$, $v_\theta(\theta) = -v_\theta(\pi - \theta)$, $v_\phi(\theta) = v_\phi(\pi - \theta)$, $c_s(\theta) = c_s(\pi - \theta)$, and $\rho(\theta) = \rho(\pi - \theta)$. Since we include the latitudinal component of the velocity, v_θ , due to even symmetric assumption, its value will be zero

at this boundary. Thus, the following boundary conditions will be imposed at $\theta = \pi/2$:

$$\frac{d\rho}{d\theta} = \frac{dc_s}{d\theta} = \frac{dv_r}{d\theta} = \frac{dv_\phi}{d\theta} = \frac{db_\phi}{d\theta} = v_\theta = 0. \quad (26)$$

We define the plasma beta which is the ratio of the gas to the magnetic pressure. To study the models with weak and strong magnetic fields, we then set its value at the equatorial plane as

$$\beta_0 = \frac{p_{\text{gas}}}{p_{\text{mag}}} = \frac{2\rho c_s^2}{b_\phi^2}. \quad (27)$$

Here, the dimensionless magnetic pressure is defined as $p_{\text{mag}} = b_\phi^2/2$. Since the maximum density is located at the equatorial plane, we adopt $\rho(\pi/2) = 1$ for all set of input parameters. By substituting the above boundary conditions into Equations (B7)–(B12), we can get the following equations at the equatorial plane

$$\frac{dv_\theta}{d\theta} = \left(n - \frac{3}{2} \right) v_r, \quad (28)$$

$$-\frac{1}{2}v_r^2 - v_\phi^2 = -1 + \left(n + 1 + \frac{n-1}{\beta} \right) c_s^2 - \alpha_2 (n-2) \left(1 + \frac{1}{\beta} \right) \left[\frac{1}{2}v_r - \frac{1}{3} \frac{dv_\theta}{d\theta} \right] c_s^2, \quad (29)$$

$$v_r = 3\alpha_1 (n-2) \left(1 + \frac{1}{\beta} \right) c_s^2, \quad (30)$$

$$\begin{aligned} \left(n - \frac{1}{\gamma-1} \right) v_r &= \frac{9}{4}\alpha_1 \left(1 + \frac{1}{\beta} \right) v_\phi^2 \\ &+ \frac{1}{2}\eta_0 (n-1)^2 \left(1 + \frac{1}{\beta} \right) c_s^2 + 3\alpha_2 \left(1 + \frac{1}{\beta} \right) \\ &\times \left[\frac{1}{2}v_r - \frac{1}{3} \frac{dv_\theta}{d\theta} \right]^2 + \kappa_0 \left(n - \frac{1}{2} + \frac{1}{c_s^2} \frac{d^2 c_s^2}{d\theta^2} \right). \end{aligned} \quad (31)$$

It is noting that without thermal conduction, i.e., $\kappa_0 = 0$, the above set of equations simply gives us the values of v_r , v_ϕ , and c_s at the equatorial plane. In the presence of the thermal conduction, we have another unknown parameter, i.e., $(d^2 c_s^2/d\theta^2)$, at the equatorial plane. To have a self-consistent solutions, we follow Khajenabi & Shadmehri 2013 approach and guess the radial velocity at the equatorial plane. We can then simply obtain the value of other physical variables such as c_s , v_ϕ and b_ϕ from Equations (28)–(30) and (27). We also impose the following physical boundary conditions

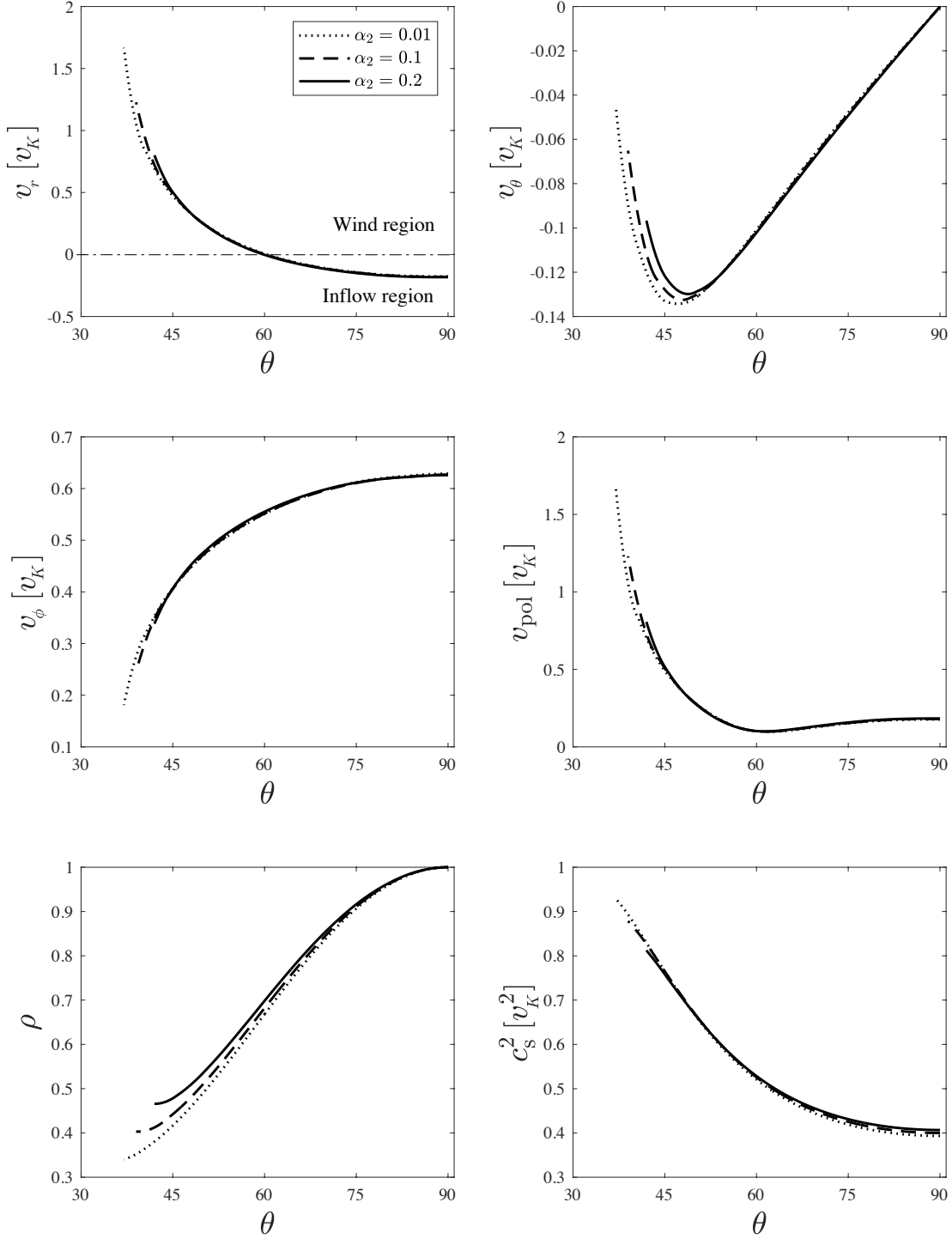


Figure 1: Latitudinal profiles of the physical variables. Top left: radial velocity, v_r , Top right: latitudinal velocity, v_θ , Middle left: angular velocity, v_ϕ , Middle right: poloidal velocity, $v_{\text{pol}} = \sqrt{v_r^2 + v_\theta^2}$, Bottom left: density, and Bottom right: sound speed squared, c_s^2 . The velocities are in the unit of Keplerian velocity, v_K , and the density is in the unit of the density at the equatorial plane. The dotted, dashed, and solid curves correspond to parameters $\alpha_2 = [0.01, 0.1, 0.2]$, respectively. Here, $\alpha_1 = 0.1$, $n = 0.5$, $\gamma = 5/3$, $\eta_0 = 0.1$, and $\beta_0 = 5000$.

at the angle where the radial velocity becomes null, i.e., $v_r(\theta_0) = 0$,

$$c_s^2(\theta_0) = \frac{\pi}{2} - \theta_0. \quad (32)$$

The above dimensionless constraint at θ_0 represents this fact that the scale-height of accretion disk, $H =$

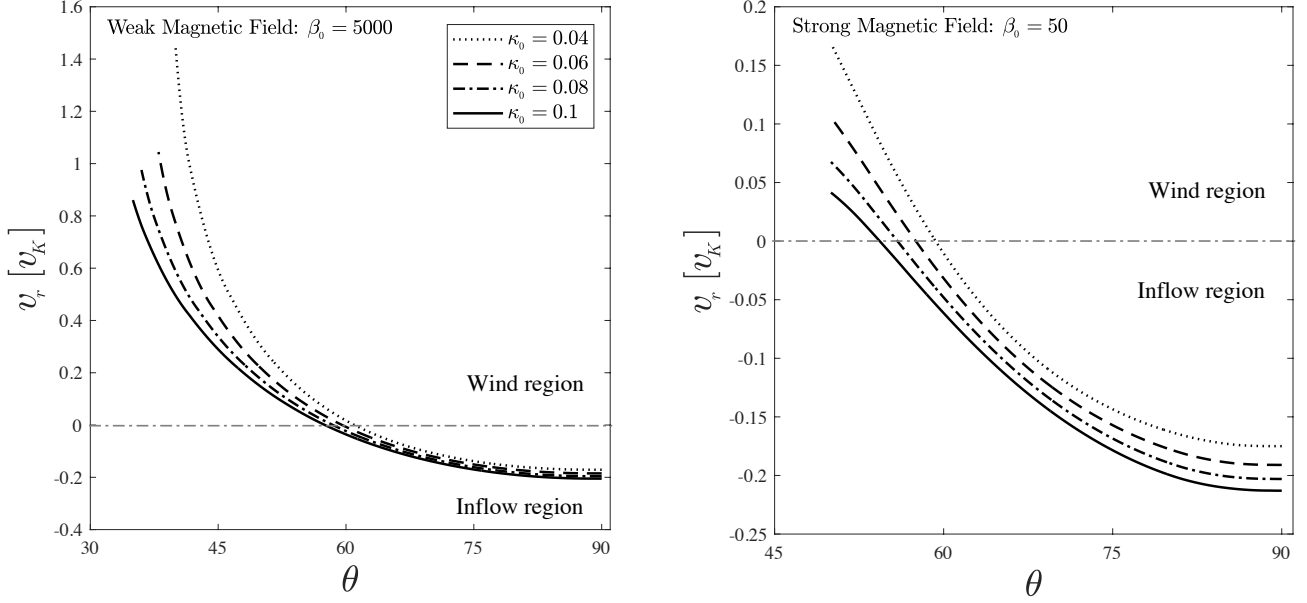


Figure 2: Latitudinal profiles of the radial velocity for four different values of $\kappa_0 = [0.04, 0.06, 0.08, 0.1]$, and for two cases of weak (left column) and strong (right column) magnetic fields. Here, $\alpha_1 = 0.1$, $\alpha_2 = 0.05$, $n = 0.5$, $\gamma = 5/3$, and $\eta_0 = 0.1$.

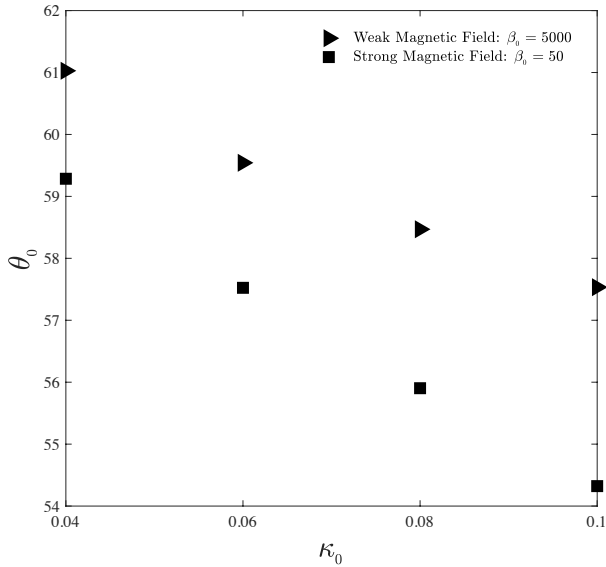


Figure 3: Opening angle θ_0 versus the thermal condition coefficient κ_0 with $\alpha_1 = 0.1$, $\alpha_2 = 0.05$, $n = 0.5$, $\gamma = 5/3$, and $\eta_0 = 0.1$. The two models with weak, $\beta_0 = 5000$, and strong magnetic fields, $\beta_0 = 50$, are marked by triangles and squares, respectively.

c_s/Ω_K should be equal to the disk height, i.e., $c_s/\Omega_K \cong (\pi/2 - \theta_0)r$. More precisely, the height of the disk is proportional to the wind temperature. By integrating the Equations (B7)- (B12), we find the angle at which the radial velocity of the flow becomes null. At this

angle we check whether the wind condition (32) at θ_0 is satisfied. If not, we choose another value for the radial velocity at the equatorial plane until the Equation (32) is satisfied. We then integrate the system of ODEs from the equatorial plane to a certain critical angle denoting as θ_B where we encounter the numerical errors. More precisely, the mass density or the gas pressure will get very close to zero at this inclination. We consider this angle as the upper boundary of the flow structure. We think that with a simple radial self-similar solution we cannot describe the flow structure near the rotation axis. The reason is as follows: if the solution does not end at an upper boundary, θ_B , the net mass accretion rate \dot{M}_{net} , at a specific radius r is calculated as,

$$\begin{aligned} \dot{M}_{\text{net}} &= \sqrt{GM} \left[4\pi \int_{\pi/2}^0 \rho(\theta) v_r(\theta) \sin \theta d\theta \right] r^{3/2-n} \\ &= 4\pi \sqrt{GM} \left[\int_{\pi/2}^{\theta_0} \rho(\theta) v_r(\theta) \sin \theta d\theta \right. \\ &\quad \left. + \int_{\theta_0}^0 \rho(\theta) v_r(\theta) \sin \theta d\theta \right] r^{3/2-n} = \dot{M}_{\text{in}} + \dot{M}_{\text{out}}. \quad (33) \end{aligned}$$

The mass conservation implies that net mass accretion rate should be a constant for a steady accretion flow. The constant mass accretion rate can only happen in the following two cases: (1) when $n = 3/2$, which forces \dot{M}_{net} not to change with radius. This case is discussed

in Narayan & Yi 1995, resulting a solution in which the flow is radial (with rotation), i.e., $v_\theta = 0$. Therefore, no outflow has been obtained in their solution. (2) When $n \neq 3/2$, the integration term in the above equation must be zero, resulting the case $\dot{M}_{\text{net}} = 0$. This requires that the outflow exactly equals the inflow at a certain radius, which in fact is not physical (no accretion process happens). Since we should have a non-zero net accretion rate, the inflow rate must be larger than the outflow rate at a certain radius, the solution must be truncated at a certain angle near the rotational axis, namely θ_B . Consequently, the solution with outflow ($n < 3/2$) cannot satisfy self-similar approximations near the rotation axis.

By adopting this method, the outflow region extends to $\theta_B < \theta < \theta_0$. We think our solution in the region of $\theta_B < \theta < \pi/2$ is physical due to this fact that the solution satisfies the equations and boundary conditions at both ends as well as $\theta = \theta_0$.

3. NUMERICAL RESULTS

To avoid a shock being caused supersonic inflow such as jet near the central region, which is a source of deviation from the radial self-similar assumptions, we neglect the region within $10r_s$. We consider radial power-law form for the physical variables to reduce the radial dependency of variables and solve the system of equations only in theta direction. Therefore, we believe our radial self-similar solutions are unique and stable. By this methodology, the PDEs are reduced to ODEs (Equations (B7)-(B12)) which we solved numerically. The equations were integrated from the equatorial plane, $\theta = \pi/2$, toward a critical angle, $\theta = \theta_B$. The solutions are in the following parameter space: $\alpha_1 = 0.1$, $\eta_0 = 0.1$, $\gamma = 5/3$, and $n = 0.5$. To explore how much the anisotropic pressure can affect the physical variables of the accretion flow, we plotted Figure 1 for three different values of $\alpha_2 = [0.01, 0.1, 0.2]$ in vertical direction and are shown by dotted, dashed, and solid lines, respectively. For this figure, $\beta_0 = 5000$ which represents weak magnetic field case². From left to right and top to bottom, it is shown the radial velocity, v_r , latitudinal velocity, v_θ , the rotational velocity, v_ϕ , the poloidal velocity, v_{pol} , the density, ρ , and the sound speed squared, c_s^2 , respectively. All velocities are plotted in the unit of Keplerian value and the density is in the unit of maximum density at the equatorial plane at that radius. It is clear that the anisotropic pressure does not considerably affect the physical quantities; however, it can decrease

the amount of the wind. For instance, in the top left panel, the wind region extends from the dot-dashed line that is $v_r = 0$ line by around $\theta \sim 35^\circ$ for $\alpha_2 = 0.01$ while for $\alpha_2 = 0.2$ this region shrinks and goes until $\theta \sim 43^\circ$. As it was easily expected, the radial velocity of the wind is much higher than that of the inflow. In the top right panel, there is an increase in the absolute value of the latitudinal velocity which the maximum amount occurs between $\theta \sim 45^\circ - 50^\circ$. Then, we can see that the absolute value of this quantity decreases toward the polar region. Therefore, the poloidal velocity of the flow shows an increasing trend from the equatorial plane toward the polar region. In the middle left panel, it is shown that v_ϕ increases with θ . The bottom left panel illustrates the density drops from the equatorial plane toward the polar region. In addition, the anisotropic pressure can increase the density especially in the wind region. This implies that as the amount of the wind is enhanced with decreasing α_2 , density decreases due to the sweeping more gas away by the wind. As you can see in the bottom right panel of figure 1, the sound speed has an increasing behavior from the disk toward the polar region.

We have not only examined the effects of the anisotropic pressure but we also investigated the influence of the thermal conductivity and the magnetic field strength on the flow properties in Figures 2, 4, and 5. In the left and right panels of Figure 2, the radial velocity is plotted for weak and strong magnetic field with $\beta = [5000, 50]$, respectively. We also consider four different values for the conductivity coefficient as $\kappa_0 = [0.04, 0.06, 0.08, 0.1]$ illustrated by dotted, dashed, dot-dashed, and solid lines, respectively. This figure clearly shows that in the weak magnetic field, thermal conduction does not affect the inflow radial velocity. However, in the case of the strong magnetic field thermal conduction can increase the inflow radial velocity. In addition, thermal conduction can decrease the radial wind velocity disregarding the magnetic field strength.

Figure 3 shows the dependency of θ_0 on κ_0 for two models with weak and strong magnetic fields, $\beta = [5000, 50]$ marked by triangles and squares, respectively. The inverse behavior of these two parameters can be clearly seen from this figure, θ_0 decreases when κ_0 increases. As θ_0 is the declination angle between inflow and wind areas, increasing κ_0 leads to a gradual shrinkage of the wind region. For the weak magnetic field the wind region is expanded respect to the strong magnetic field. For instance, for $\kappa = 0.06$ the wind region in weak magnetic field starts from $\theta \sim 61^\circ$ while in strong magnetic field it starts from $\theta \sim 59^\circ$.

² We also examin anisotropic pressure effects for strong magnetic field case and the results were almost identical to Figure 1

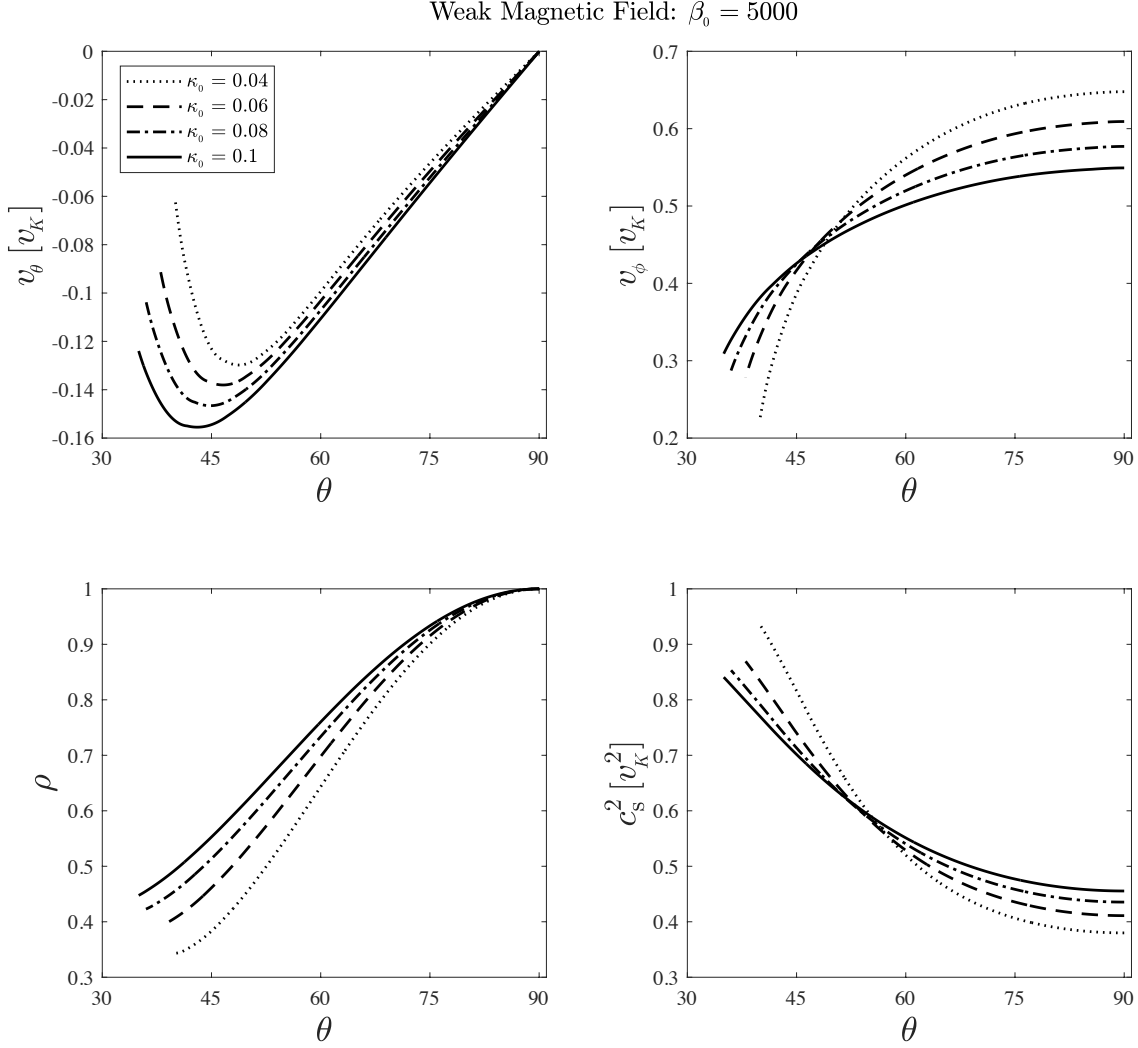


Figure 4: Latitudinal profiles of the physical variables for weak magnetic field, $\beta_0 = 5000$. Top left: latitudinal velocity, v_θ ; Top right: rotational velocity, v_ϕ ; Bottom left: density, and Bottom right: sound speed squared, c_s^2 . The dotted, dashed, dot-dashed and solid curves correspond to parameters $\kappa_0 = [0.04, 0.06, 0.08]$ and 0.1, respectively. Here, $\alpha_1 = 0.1$, $\alpha_2 = 0.05$, $n = 0.5$, $\gamma = 5/3$, and $\eta_0 = 0.1$.

The impact of the thermal conduction on other physical variables of the accretion flow in two weak and strong magnetic field models, $\beta = [5000, 50]$, is examined in Figures 4 and 5, respectively. Latitudinal velocity in the unit of Keplerian value is plotted in the top left panel of Figure 4. Although the thermal conduction does not show any effects on v_θ around the equatorial plane, it causes the absolute value of wind latitudinal velocity increases. In the case of the strong magnetic field in Figure 5, the absolute value of the latitudinal velocity drastically increases toward the polar region. In the top right panel of Figure 4 it is seen that when magnetic field is weak, thermal conductivity shows a different effect on the rotational velocity of the inflow and wind. In the inflow, the thermal conductivity reduces the rotational

velocity however it can increase the wind velocity. We cannot see this inverse behavior in the inflow and wind region when the magnetic field magnifies. In the case of strong magnetic field, thermal conduction causes a decrease in the rotational velocity of both inflow and wind (top right panel of Figure 5). In both cases of the magnetic field the density increases with the thermal conduction and this implies that the thermal conduction can make the disk thicker. In addition, in the weak magnetic field the density drops smoother rather than the case with strong magnetic field (bottom left panels of Figures 4 and 5). The sound speed squared in the unit of Keplerian velocity is plotted in the bottom right panel of both Figures 4 and 5. A comparison between these two panels shows that thermal conduction can re-

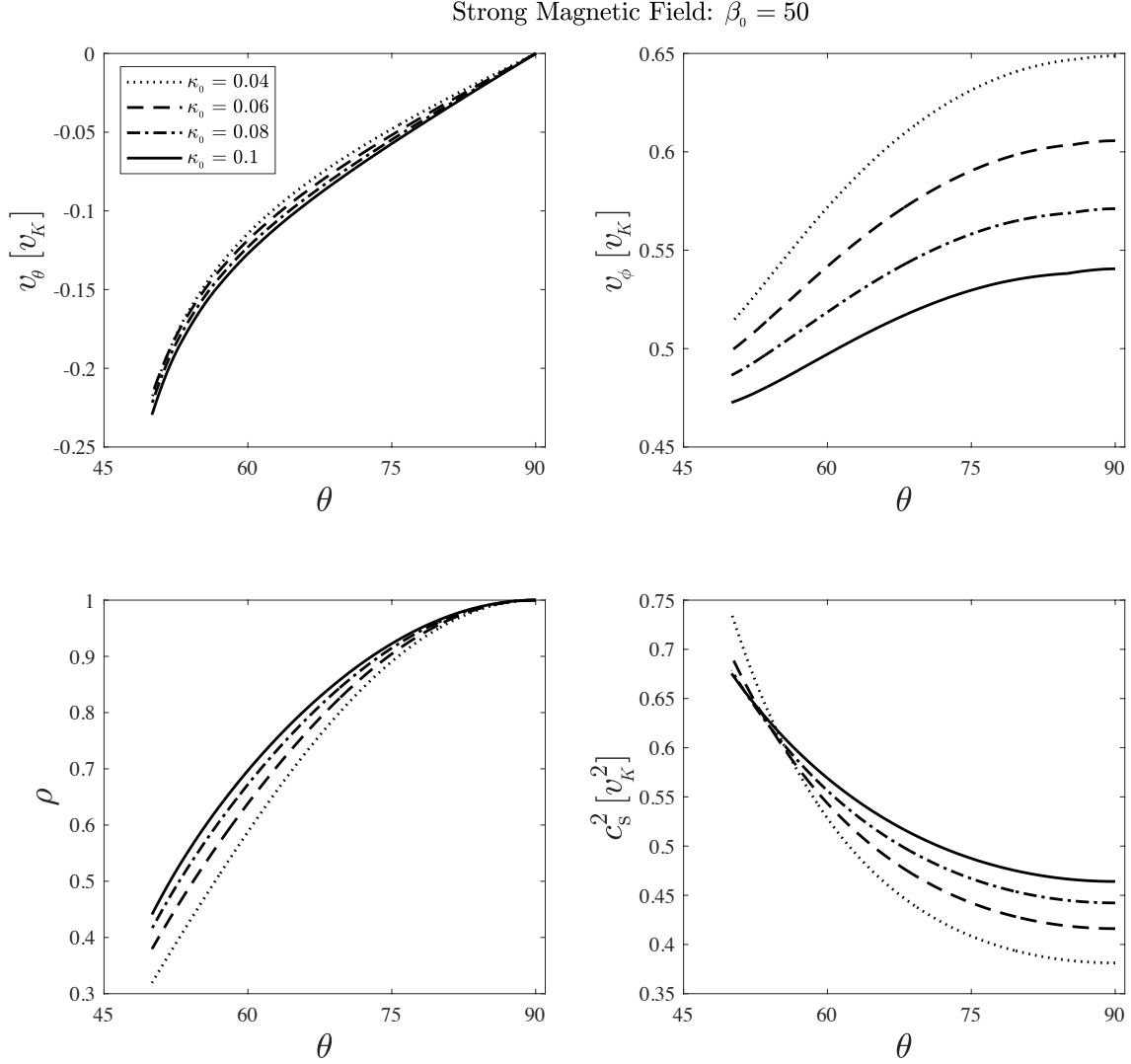


Figure 5: Latitudinal profiles of the physical variables for strong magnetic field, $\beta_0 = 50$. Top left: latitudinal velocity, v_θ ; Top right: rotational velocity, v_ϕ ; Bottom left: density, and Bottom right: sound speed squared, c_s^2 . The dotted, dashed, dot-dashed and solid curves correspond to parameters $\kappa_0 = [0.04, 0.06, 0.08]$ and 0.1, respectively. Here, $\alpha_1 = 0.1$, $\alpha_2 = 0.05$, $n = 0.5$, $\gamma = 5/3$, and $\eta_0 = 0.1$.

duce the sound speed and thus the temperature of the flow. Further, it can be seen that for the higher values of the thermal conduction the sound speed increases smoothly from the equatorial plane toward the polar region. More, when the magnetic field strength increases the sound speed decreases in the wind region.

The Bernoulli parameter with only considering toroidal magnetic field is defined as

$$\text{Be} = \frac{1}{2}v^2 + h + \psi + \frac{B_\phi^2}{4\pi\rho} \quad (34)$$

where $h(= \gamma p / [\rho(\gamma - 1)])$ is enthalpy. The top row panels of Figure 6 show the Bernoulli parameter for four values of the conductivity coefficients, $\kappa = [0.04, 0.06, 0.08, 0.1]$,

and also for weak and strong magnetic fields, $\beta = [5000, 50]$, respectively. As you can see, enthalpy is higher in the weak magnetic field with respect to the strong magnetic field. However, we cannot see significant changes in the Bernoulli parameter when the strength of the magnetic field is amplified.

We also calculated the wind power which includes kinetic, thermal, and Poynting energy fluxes as

$$P_k(r) = 2\pi r^2 \int_{0^\circ}^{90^\circ} \rho \max(v_r^3, 0) \sin \theta d\theta, \quad (35)$$

$$P_{\text{th}}(r) = 4\pi r^2 \int_{0^\circ}^{90^\circ} \rho e \max(v_r, 0) \sin \theta d\theta, \quad (36)$$

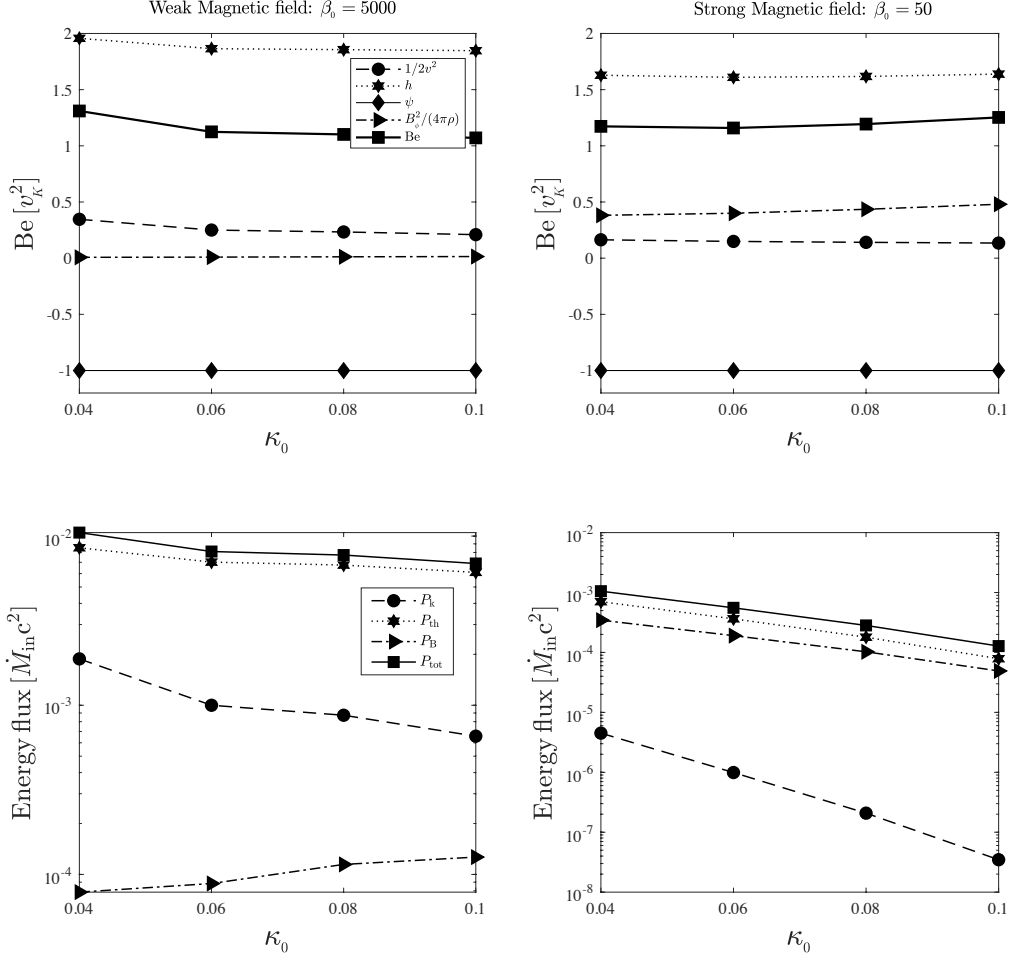


Figure 6: Bernoulli parameter (top row panels) and energy flux (bottom row panels) for four different values of $\kappa_0 = [0.04, 0.06, 0.08, 0.1]$, and for two cases of weak (left column) and strong (right column) magnetic fields.

$$P_B(r) = 4\pi r^2 \int_{0^\circ}^{90^\circ} S_r \max(v_r/|v_r|, 0) \sin\theta d\theta. \quad (37)$$

where S_r is the radial component of Poynting flux and is defined as

$$S_r = v_r \frac{B_\phi^2}{4\pi}. \quad (38)$$

The results are plotted in the bottom row of Figure 6 with respect to the conductivity coefficient where the left and right panels are for weak and strong magnetic fields, respectively. All components of the energy flux decrease with the conductivity coefficient in both cases of the magnetic field except for the Poynting energy flux in the weak magnetic field which increases with this parameter. Clearly, the thermal energy flux dominates two other fluxes in both weak and strong magnetic field cases. Moreover, when the magnetic field is weak the

kinetic energy flux is larger than the Poynting energy flux. As the magnetic field magnifies, the Poynting energy flux prevails over the kinetic energy.

4. SUMMARY AND DISCUSSION

In this paper, we solve the equations of the hot accretion flow by considering magnetic field, anisotropic pressure and thermal conduction. We investigate the properties of the inflow and wind of the collisionless plasmas in hot accretion flows with very low mass accretion rates. As increase or decrease in the magnetic field strength makes a pressure anisotropy, we compare the physical quantities of the accretion flow in two cases with weak and strong magnetic field. We decompose the magnetic field into a large-scale component and a turbulent component. We only consider toroidal component of magnetic field. The effects of turbulence are described by the viscosity. Both components can transfer the an-

gular momentum outward and produce heat. We modeled the anisotropic pressure with an anisotropic viscosity. By considering the self-similar solutions, we solved the ODEs numerically. We examined the anisotropic pressure on the properties of the inflow and wind. Our results showed that the increase of the anisotropic pressure tends to give rise to shrink the wind region. We also investigate the effects of the thermal conduction and the magnetic field strength on the properties of the inflow and wind. We found that the impact of the thermal conductivity on the flow to some extent depends on the magnetic field strength. As in the strong magnetic field, thermal conduction tends to decrease the rotational velocity of the wind. Thermal conductivity also tends to shrink the wind region. Our results showed that neither thermal conduction nor the magnetic field strength can impressively impact on the Bernoulli parameter. We explored the energy flux of the wind in details to know how thermal conduction and the magnetic field strength can affect the thermal, kinetic, and Poynting energy fluxes. We found that, except the Poynting energy flux, the thermal conduction can decrease all components of the energy flux in both weak and strong magnetic fields. What is more, the strength of the magnetic field can help the Poynting energy flux overcomes the kinetic en-

ergy flux. In terms of black hole mass, the main application of our hot accretion results is in the dim black hole sources, including the supermassive black hole in our Galactic center, low-luminosity active galactic nuclei (AGNs), and quiescent and hard states of black hole X-ray binaries. Additional physics, namely, radiative cooling and self-gravity can play a significant role to construct realistic physical models. These additional physics may not necessarily allow a self-similar solution. But in some cases, they can help to determine some of the parameters of the self-similar model.

- 1 A.M. is supported by the China Postdoctoral Science
- 2 Foundation (grant No. 2020M673371). F.Z.Z. is sup-
- 3 ported by the National Natural Science Foundation of
- 4 China (grant No. 12003021) and also the China Post-
- 5 doctoral Science Foundation (grant No. 2019M663664).
- 6 L.M. is supported by the National Natural Science Foun-
- 7 dation of China (grant No. 12171385). A.M. also ac-
- 8 knowledges the support of Dr. X. D. Zhang at the Net-
- 9 work Information Center of Xi'an Jiaotong University.
- 10 The computation has made use of the High Performance
- 11 Computing (HPC) platform of Xi'an Jiaotong Univer-
- 12 sity.

APPENDIX

A. PARTIAL DIFFERENTIAL EQUATIONS IN SPHERICAL COORDINATES

To simplify the set of equations (1)-(5), we consider the flow is in steady-state and axisymmetric ($\partial/\partial t = \partial/\partial\phi = 0$). Spherical polar coordinate system (r, θ, ϕ) is adopted. We assume all components of the velocity field, $\mathbf{v} = v_r\hat{r} + v_\theta\hat{\theta} + v_\phi\hat{\phi}$. We further assume only the toroidal component of magnetic field is presented. By substituting all assumptions and definitions introduced in subsection 2.1 into equations (1)-(5), we obtain following partial differential equations (PDE). Hence, the continuity equation is reduced to the following form,

$$\frac{1}{r^2} \frac{\partial}{\partial r} (r^2 \rho v_r) + \frac{1}{r \sin \theta} \frac{\partial}{\partial \theta} (\rho v_\theta \sin \theta) = 0. \quad (\text{A1})$$

The three components of the momentum equation are as,

$$\rho \left[v_r \frac{\partial v_r}{\partial r} + \frac{v_\theta}{r} \left(\frac{\partial v_r}{\partial \theta} - v_\theta \right) - \frac{v_\phi^2}{r} \right] = -\frac{GM\rho}{r^2} - \frac{\partial p_{\text{gas}}}{\partial r} + \frac{J_\theta B_\phi}{4\pi} + \frac{1}{r^2} \frac{\partial}{\partial r} (r^2 \Pi_{rr}) - \frac{1}{r} (\Pi_{\theta\theta} + \Pi_{\phi\phi}), \quad (\text{A2})$$

$$\rho \left[v_r \frac{\partial v_\theta}{\partial r} + \frac{v_\theta}{r} \left(\frac{\partial v_\theta}{\partial \theta} + v_r \right) - \frac{v_\phi^2}{r} \cot \theta \right] = -\frac{1}{r} \frac{\partial p_{\text{gas}}}{\partial \theta} - \frac{J_r B_\phi}{4\pi} + \frac{1}{r \sin \theta} \frac{\partial}{\partial \theta} (\sin \theta \Pi_{\theta\theta}) - \frac{\Pi_{\phi\phi}}{r} \cot \theta, \quad (\text{A3})$$

$$\rho \left[v_r \frac{\partial v_\phi}{\partial r} + \frac{v_\theta}{r} \frac{\partial v_\phi}{\partial \theta} + \frac{v_\phi}{r} (v_r + v_\theta \cot \theta) \right] = \frac{1}{r^3} \frac{\partial}{\partial r} (r^3 \sigma_{r\phi}). \quad (\text{A4})$$

The energy equation is driven as,

$$\rho \left(v_r \frac{\partial e}{\partial r} + \frac{v_\theta}{r} \frac{\partial e}{\partial \theta} \right) - \frac{p_{\text{gas}}}{\rho} \left(v_r \frac{\partial \rho}{\partial r} + \frac{v_\theta}{r} \frac{\partial \rho}{\partial \theta} \right) = \sigma_{r\phi} r \frac{\partial}{\partial r} \left(\frac{v_\phi}{r} \right) + \frac{\eta}{4\pi} (J_r^2 + J_\theta^2) + \frac{1}{r^2} \frac{\partial}{\partial r} \left(r^2 \kappa \frac{\partial T}{\partial r} \right) + \frac{1}{r \sin \theta} \frac{\partial}{\partial \theta} \left(\frac{\kappa \sin \theta}{r} \frac{\partial T}{\partial \theta} \right) - \Pi_{rr} \frac{\partial v_r}{\partial r} - \frac{\Pi_{\theta\theta}}{r} \left(\frac{\partial v_\theta}{\partial \theta} + v_r \right) - \frac{\Pi_{\phi\phi}}{r} (v_r + v_\theta \cot \theta). \quad (\text{A5})$$

Finally, the induction equation will be written as follows,

$$\frac{\partial}{\partial r} (r v_r B_\phi) + \frac{\partial}{\partial \theta} (v_\theta B_\phi) - \frac{\partial}{\partial \theta} (\eta J_r) + \frac{\partial}{\partial \theta} (r \eta J_\theta) = 0. \quad (\text{A6})$$

B. ORDINARY DIFFERENTIAL EQUATIONS

The ordinary differential equations (ODEs) can be derived just by substituting self-similar solutions presented in section 2.2 into the partial differential equations (A1)–(A6) as,

$$\rho \left[\left(\frac{3}{2} - n \right) v_r + \frac{dv_\theta}{d\theta} + v_\theta \cot \theta \right] + v_\theta \frac{d\rho}{d\theta} = 0, \quad (\text{B7})$$

$$\rho \left[-\frac{1}{2} v_r^2 + v_\theta \frac{dv_r}{d\theta} - v_\theta^2 - v_\phi^2 \right] = -\rho + (n+1) p_{\text{gas}} + j_\theta b_\phi - \alpha_2 p_{\text{tot}} (n-2) \left[\frac{1}{2} v_r + \frac{2}{3} v_\theta \cot \theta - \frac{1}{3} \frac{dv_\theta}{d\theta} \right], \quad (\text{B8})$$

$$\rho \left[\frac{1}{2} v_r v_\theta + v_\theta \frac{dv_\theta}{d\theta} - v_\phi^2 \cot \theta \right] = -\frac{dp_{\text{gas}}}{d\theta} - j_r b_\phi + \alpha_2 \left(\frac{dp_{\text{tot}}}{d\theta} + 3p_{\text{tot}} \cot \theta \right) \left[\frac{1}{2} v_r + \frac{2}{3} v_\theta \cot \theta - \frac{1}{3} \frac{dv_\theta}{d\theta} \right] + \alpha_2 p_{\text{tot}} \left[\frac{1}{2} \frac{dv_r}{d\theta} + \frac{2}{3} \left(\frac{dv_\theta}{d\theta} \cot \theta - v_\theta \csc^2 \theta \right) - \frac{1}{3} \frac{d^2 v_\theta}{d\theta^2} \right], \quad (\text{B9})$$

$$\rho \left[\frac{1}{2} v_r v_\phi + v_\theta \frac{dv_\phi}{d\theta} + v_\theta v_\phi \cot \theta \right] = \frac{3}{2} \alpha_1 (n-2) p_{\text{tot}} v_\phi, \quad (\text{B10})$$

$$\left(n - \frac{1}{\gamma - 1} \right) v_r p_{\text{gas}} + \frac{v_\theta}{\gamma - 1} \left(\frac{dp_{\text{gas}}}{d\theta} - \gamma \frac{p_{\text{gas}}}{\rho} \frac{d\rho}{d\theta} \right) = \frac{9}{4} \alpha_1 p_{\text{tot}} v_\phi^2 + \eta (j_r^2 + j_\theta^2) + 3\alpha_2 p_{\text{tot}} \left(\frac{1}{2} v_r + \frac{2}{3} v_\theta \cot \theta - \frac{1}{3} \frac{dv_\theta}{d\theta} \right)^2 + \kappa_0 \left[\left(n - \frac{1}{2} \right) c_s^2 + \frac{1}{\sin \theta} \frac{d}{d\theta} \left(\sin \theta \frac{dc_s^2}{d\theta} \right) \right], \quad (\text{B11})$$

$$\frac{n}{2} v_r b_\phi - v_\theta \frac{db_\phi}{d\theta} - b_\phi \frac{dv_\theta}{d\theta} + \eta \frac{dj_r}{d\theta} + j_r \frac{d\eta}{d\theta} + \frac{n}{2} \eta j_\theta = 0, \quad (\text{B12})$$

where

$$p_{\text{gas}} = \rho c_s^2 \quad (\text{B13})$$

$$p_{\text{tot}} = p_{\text{gas}} + p_{\text{mag}} \quad (\text{B14})$$

$$p_{\text{mag}} = \frac{b_\phi^2}{2} \quad (\text{B15})$$

$$j_r = \frac{db_\phi}{d\theta} + b_\phi \cot \theta, \quad (\text{B16})$$

$$j_\theta = \frac{1}{2} (n-1) b_\phi, \quad (\text{B17})$$

$$\eta = \eta_0 \frac{p_{\text{tot}}}{\rho}. \quad (\text{B18})$$

REFERENCES

- Abbassi, S., Ghanbari, J., & Najjar, S. 2008, *MNRAS*, 388, 663
- Akizuki, C., & Fukue, J. 2006, *PASJ*, 58, 469
- Balbus, S. A. 2004, *ApJ*, 616, 857
- Balbus, S. A., & Hawley, J. F. 1991, *ApJ*, 376, 214
- Balbus, S. A., & Hawley, J. F. 1998, *Rev. Mod. Phys.*, 70, 1
- Begelman, M. C., McKee, C. F., & Shields, G. A. 1983, *ApJ*, 271, 70
- Blandford, R. D., & Payne, D. G. 1982, *MNRAS*, 199, 883
- Braginskii S. I. 1965, *Rev. Plasma Phys.*, 1, 205
- Bu, D. F., & Mosallanezhad, A. 2018, *A&A*, 615, A35
- Bu, D. F., Yuan, F., Xie, F. G. 2009, *MNRAS*, 392, 325
- Bu D. F., Gan Z. M., 2018, *MNRAS*, 474, 1206
- Chandra, M., Gammie, C. F., Foucart, F., & Quataert, E. 2015, *ApJ*, 810, 162
- Cheung, E., Bundy, K., Cappellari, M., Peirani, S., Rujopakarn, W., Westfall, K., Yan, R., Bershad, M., Greene, J.E., Heckman, T.M., et al., 2016, *Nature*, 533, 504
- Crenshaw, D. M. & Kraemer, S. B., 2012, *ApJ*, 753, 75
- De Villiers, J.-P., Hawley, J. F., & Krolik, J. H. 2003, *ApJ*, 599, 1238
- De Villiers, J.-P., Hawley, J. F., Krolik, J. H., & Hirose, S. 2005, *ApJ*, 620, 878
- Deng, H.-H., Bu, D.-F. 2019, *Universe*, 5, 197D
- Fabian, A. C. 2012, *ARA&A*, 50, 455
- Font, A. S., McCarthy, I. G., Johnstone, D., & Ballantyne, D. R. 2004, *ApJ*, 607, 890
- Hawley, J. F., & Balbus, S. A. 2002, *ApJ*, 573, 738
- Hawley, J., Balbus, S. A., & Stone, J. M. 2001, *ApJ*, 554, L49
- Igumenshchev, I. V., & Abramowicz, M. A. 1999, *MNRAS*, 303, 309
- Igumenshchev, I. V., & Abramowicz, M. A. 2000, *ApJS*, 130, 463
- Igumenshchev, I. V., Narayan, R. 2002, *ApJ*, 566, 137
- Igumenshchev, I. V., Narayan, R., & Abramowicz, M. A. 2003, *ApJ*, 592, 1042
- Inayoshi, K., Ostriker, J. P., Haiman, Z., & Kuiper, R. 2018, *MNRAS*, 476, 1412
- Inayoshi, K., Ichikawa, K., Ostriker, J. P., & Kuiper, R. 2019, *MNRAS*, 486, 5377
- Khajenabi, F., & Shadmehri, M. 2013, *MNRAS*, 436, 2666
- Kormendy J. & Ho, L. 2013, *ARA&A*, 51, 511
- Li, J., Ostriker, J., & Sunyaev, R. 2013, *ApJ*, 767, 105L
- Luketic, S., Proga, D., Kallman, T. R., Raymond, J. C., & Miller, J. M. 2010, *ApJ*, 719, 515
- Lynden-Bell, D. 1996, *MNRAS*, 279, 389
- Lynden-Bell, D. 2003, *MNRAS*, 341, 1360
- Ma, M., Roberts, S.R., Li, Y., Wang, Q.D., 2019, *MNRAS*, 483, M5614
- Machida, M., Matsumoto, R., & Mineshige, S. 2001, *PASJ*, 53, L1
- McKinney, J., Tchekhovskoy, A., & Blandford, R. 2012, *MNRAS*, 423, 3083
- Mosallanezhad, A., Abbassi, S., & Beiranvand, N. 2014, *MNRAS*, 437, 3112
- Murray, N., Chiang, J., Grossman, S. A., & Voit, G. M. 1995, *ApJ*, 451, 498
- Naab, T., & Ostriker, J. P. 2017, *ARA&A*, 55, 59
- Narayan, R., & Yi, I. 1995, *ApJ*, 452, 710
- Narayan, R., & Yi, I. 1994, *ApJ*, 428, L13
- Narayan, R., Mahadevan, R., & Quataert, E. 1998, in *The Theory of Black Hole Accretion Discs*, ed. M. A. Abramowicz, G. Bjornsson, & J. E. Pringle (Cambridge: Cambridge Univ. Press)
- Narayan, R., Sadowski, A., Penna, R. F., & Kulkarni, A. K. 2012, *MNRAS*, 426, 3241
- Nomura, M., & Ohsuga, K. 2017, *MNRAS*, 465, 2873
- Pang, B., Pen, U. L., Matzner, C. D., Green, S. R., & Liebendörfer, M. 2011, *MNRAS*, 415, 1228
- Pen, U.-L., Matzner, C. D., & Wong, S. 2003, *ApJ*, 596, L207
- Proga, D., Stone, J. M., Kallman, T. R. 2000, *ApJ*, 543, 686
- Proga, D., & Kallman, T. R. 2004, *ApJ*, 616, 688
- Quataert, E. 2003, *Astron. Nachr./AN*, 324, 435
- Samadi, M., Abbassi, S., & Lovelace, R. V. E. 2017, *MNRAS*, 470, 2018
- Shakura, N. I., & Sunyaev, R. A. 1973, *A&A*, 24, 337
- Stone, J. M., & Pringle, J. E. 2001, *MNRAS*, 322, 461
- Stone, J. M., Pringle, J. E., & Begelman, M. C. 1999, *MNRAS*, 310, 1002
- Tanaka, T., & Menou, K. 2006, *ApJ*, 649, 345
- Tombesi, F., Sambruna, J. N., Braitto, V., Ballo, L., Gofford, J., Cappi, M., Mushotzky, R. F. 2010, *ApJ*, 719, 700
- Tombesi, F., Tazaki, F., Mushotzky, R. F., Ueda, Y., Cappi, M., Gofford, J., Reeves, J. N., Guainazzi, M., 2014, *MNRAS*, 443, 2154-2182
- Wang, Q.D., Nowak, M.A., Markoff, S.B., Baganoff, F.K., Nayakshin, S., Yuan, F., Cuadra, J., Davis, J., Dexter, J., Fabian, A.C., et al., 2013, *Science*, 341, 981-983
- Waters, T. R., & Proga, D. 2012, *MNRAS*, 426, 2239
- Yuan, F., & Bu, D. 2010, *MNRAS*, 408, 1051
- Yuan, F., Narayan, R. 2014, *ARA&A*, 52, 529
- Yuan, F., Bu, D., Wu, M. 2012a, *ApJ*, 761, 130
- Yuan, F., Wu, M., & Bu, D. 2012b, *ApJ*, 761, 129

- Yuan, F., Gan, Z. M., Narayan, R., Sadowski, A., Bu, D., & Bai, X. N. 2015, *ApJ*, 804, 101
- Zhang, D., & Dai, Z. G. 2008, *MNRAS*, 388, 1409